Supplementary information for "Epitaxially ferroelectric hexagonal boron nitride on graphene"

Sheng-Shong Wong[1,2], Zhen-You Lin[1], Sheng-Zhu Ho[1], Chin-En Hsu[3], Ping-Hung Li[1], Ching-Yu Chen[1], Yen-Fu Huang[1], Chia-Hao Chen[2,4], Yi-Chun Chen[1,7*], Hung-Chung Hsueh[3*], Cheng-Maw Cheng[2,4,5,6*], and Chung-Lin Wu[1,2,7*]

[1]*Department of Physics, National Cheng Kung University, Tainan 70101, Taiwan*
[2]*National Synchrotron Radiation Research Center (NSRRC), Hsinchu 30076, Taiwan*
[3]*Department of Physics, Tamkang University, New Taipei City 251301, Taiwan*
[4]*Department of Electrophysics, National Yang Ming Chiao Tung University, Hsinchu 300 Taiwan.*
[5]*Department of Physics, National Sun Yat-sen University, Kaohsiung 80424, Taiwan*
[6]*Taiwan Consortium of Emergent Crystalline Materials, National Science and Technology Council, Taipei 10601, Taiwan.*
[7]*Center for Quantum Frontiers of Research and Technology (QFort), National Cheng Kung University, Tainan 70101, Taiwan*

[*] Email: ycchen93@mail.ncku.edu.tw, hchsueh@gms.tku.edu.tw, makalu@nsrrc.org.tw, and clwuphys@mail.ncku.edu.tw

S1. Surface characterization of epitaxial hBN

S1.1. *in situ* RHEED characterization of h-BN and crystalline graphene grown on the SiC (0001) substrate

In previous studies on epitaxial graphene on SiC, the $6\sqrt{3} \times 6\sqrt{3}\ R30°$ surface reconstruction is a well-known result, where graphene epitaxially grows on SiC with a rotational angle of 30° along the long axis [1]. According to our *in situ* RHEED characterization, h-BN grown on graphene does not exhibit reconstruction and it is along the same crystalline axis because the difference in lattice constants between them is too small to achieve reconstruction. The RHEED diffraction patterns (upper panel in Fig. S1a) with the black line representing the short axis of graphene and the red line representing the long axis of SiC. The additional tiny diffraction lines indicate the $6\sqrt{3} \times 6\sqrt{3}\ R30°$ surface reconstruction. The ratio of the SiC long axis to the graphene short axis (lower panel in Fig. S1a) matches their ratio in real space. The tiny diffraction lines represent a long period in the real space, corresponding to thirteen graphene short-axis lattices and eighteen SiC long-axis lattices. The other high-symmetry diffraction facet (Fig. S1b), where the black and red lines represent the long axis of graphene and the short axis of SiC, respectively. It should be noted that there is no change in the RHEED pattern after monolayer h-BN is grown on the graphene/SiC substrate. According to the results of RHEED diffraction patterns (Figs. S1a and S1b), the relative crystalline orientations of h-BN, graphene, and the SiC substrate are determined (Fig. S1c). Furthermore, following the analysis of the RHEED pattern and the crystalline orientations of the h-BN/graphene/SiC system, we depict the ball model over a long period under an ideal relaxed stacking condition (Fig. S1d). In real space, the length of the thirteen graphene long-axis lattices (b, black) is nearly the same as that of the eighteen SiC short-axis lattices (a*, purple) in the $<\bar{2}100>$ direction. On the other hand, the length of the thirteen graphene short-axis lattices (b*, green) is nearly the same as that of the six SiC long-axis lattices (a, red) in the $<01\bar{1}0>$ direction, thus permitting R30° $6\sqrt{3}\times6\sqrt{3}$ surface reconstruction. The ratio of b to a* is 1.387, which is similar to the diffraction result (Fig. S1a), the ratio of the graphene long axis to the SiC short axis in the RHEED diffraction pattern along the $<01\bar{1}0>$ direction is 1.369. On the other hand, the ratio of b* to a is 0.462, is similar to the diffraction result (Fig. S1b), the ratio of the graphene long axis to the SiC short axis in the RHEED diffraction pattern along the $<\bar{2}100>$ direction is 0.474.

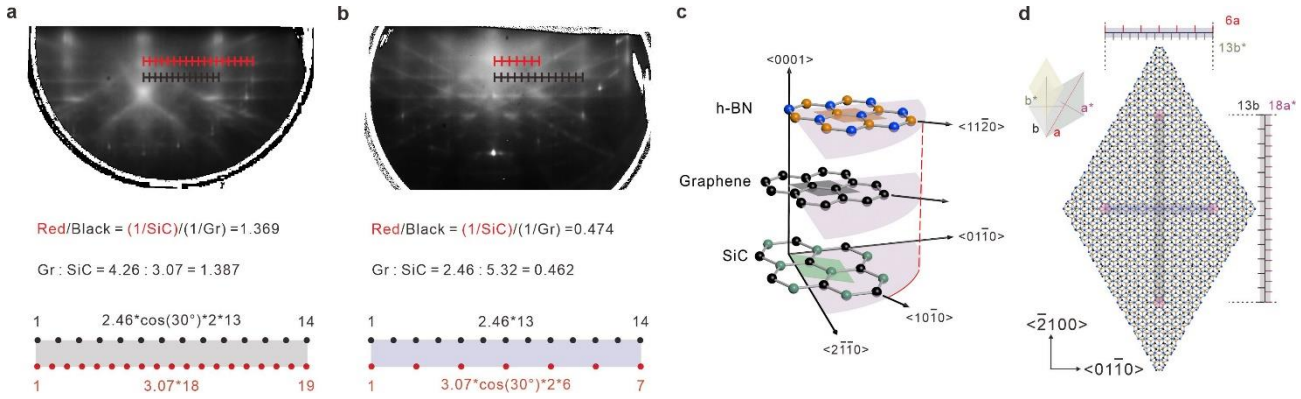

Figure S1 | RHEED pattern analysis of the epitaxially grown h-BN on graphene/SiC. a, RHEED patterns of the long-axis h-BN/graphene (red) and short-axis SiC (black); their length ratio (red/black) is 1.369, which is similar to that of the h-BN/graphene short axis to the SiC long axis in the real space, 1.387. **b**, RHEED patterns of the short-axis h-BN/graphene (red) and long-axis SiC (black); their length ratio (red/black) is 0.474, which is similar to that of the h-BN/graphene long axis to the SiC short axis in real space, 0.462. **c**, Crystal orientation of each layer in the epitaxial h-BN/graphene/SiC layer structure. **d**, h-BN/graphene/SiC top view. The rhombuses on the left side represent the SiC (green), graphene (grey), and h-BN (yellow) lattices and the SiC long and short axes are indicated by (red) and a* (purple), respectively, and the graphene long and short axes are indicated by b (black) and b* (green), respectively.

S1.2. Topographic imaging of the lattice-mismatched h-BN (mono- and bilayer)/Graphene Heterojunction

The 4° miscut angle of the 4H-SiC substrate results in a high-density saw-toothed surface morphology with one side of each tooth having a waning slope and the other having a steep slope. In our experiment, a 4° miscut angle is a relatively small angle such that the waning slope side can extend to a few micrometers in length, accompanied by a sharp steep slope covering the whole substrate surface along the $[11\bar{2}0]$ direction (step edge perpendicular to the $[11\bar{2}0]$ direction). During the graphene growth process, silicon atoms diffuse and evaporate from the step edge, leaving behind carbon atoms; these atoms then self-assemble into a 2D carbon membrane, namely graphene. As the step edge is the favorable nucleation site for h-BN, a high-density step-edge graphene substrate is crucial for the large-scale growth of h-BN. Based on the study of epitaxy of graphene on a SiC substrate, an appropriate silicon evaporation rate yields a regular-sized step edge during the graphene growth process. We decrease the evaporation rate of silicon atoms by lowering the growth temperature and prolonging the growth time. In comparison to high growth temperature conditions, in low growth temperature conditions, the gently diffused silicon atoms exhibit a higher possibility to evaporate from the waning slope side instead of the steep slope side. Therefore, the graphene still retains the saw-toothed surface morphology (200–300 nm for each step), but each waning slope side leads to a high number of fragments with a fine saw-toothed surface morphology (20–100 nm for each step). Comparing the mono- and bilayer h-BN on the graphene substrate (Fig. S2a and S2b), the 500×500 nm scale only shows one or two regular steps; hence, the left side of monolayer h-BN on graphene substrate (Fig. S2a) shows the end point of the steep slope side and the start point of the waning slope side, and the waning slope side keeps ramping toward the right for ~400 nm and then becomes the steep slope side. Because of the low silicon evaporation rate, a number of fine saw-toothed shapes in regular steps are observed. However, these tiny steps are beneficial for the large-scale growth of h-BN, and the step height is too high for the height difference in the vdW materials, causing the h-BN islands to be almost indistinguishable in the AFM topography image. Fortunately, the height for each step perpendicular to the ramping direction is the same; hence, h-BN on graphene through the cross-line profile is still found to be parallel to the step edge, and the height difference is in agreement with the van der Waals epitaxy (Fig. S2c). The cAFM current and PFM amplitude images for monolayer h-BN on graphene at a scale of 76×76 nm (Fig. S2d and S2e), both images correspond to the built-in polarization field induced by different stacking forms of h-BN/graphene, which is mentioned in the

main text. As a result, both show a moiré lattice with a 14 nm period (Fig. S2f).

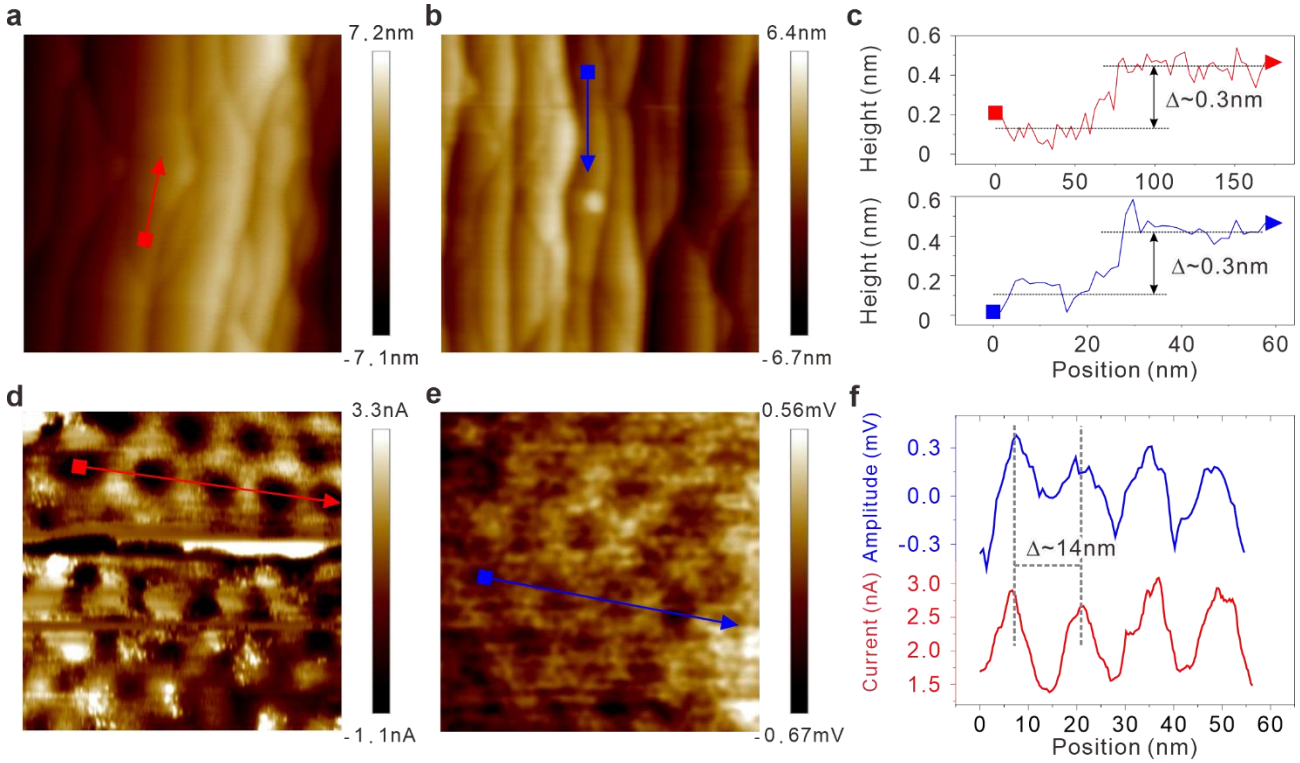

Figure S2 | Topography image of layer-controlled hBN. Topographic images of **a**, monolayer h-BN on graphene and **b**, bilayer h-BN on monolayer h-BN at a scale of 500 × 500 nm. **c**, Line profiles of the heights in **a** and **b**, given by the red line and blue line, respectively; this indicates that the height difference in each layer is approximately 0.3 nm, which corresponds to the van der Waals epitaxial growth. **d**, cAFM and **e**, PFM images of monolayer h-BN on graphene at a scale of 76 × 76 nm. **f**, Line profiles of the current in **d** and amplitude in **e**, given by the red line and blue line, respectively, both showing the moiré lattice with a 14-nm period.

S1.3. Analysis of the cAFM moiré pattern image with simulated interlayer charge transfer between h-BN and graphene

Because of the large ramping slope from a 4° miscut angle of the 4H-SiC substrate, it is challenging to investigate crystalline details on the monolayer-h-BN/graphene surface using typical AFM morphology measurement. Here, we found that the moiré pattern induced by different stacking configurations between monolayer h-BN and graphene is clearly observed by conductive AFM (cAFM) and piezoelectric force microscopy (PFM) techniques. Based on our first-principles calculations (method) different interlayer charge transfer scenarios in AB_B and AB_N stackings can be illustrated by interlayer differential charge density distributions as shown in Fig. S3a and S3b, respectively. In the case of AB_B stacking characterized by arranging B atoms atop of the hexagonal centers of graphene and stacking N atoms on the top of C atoms, the unbalanced atomic electronegativities between h-BN and graphene layers trigger an interlayer charge migration (as shown in Fig. S3c) to form an upward out-of-plane polarization of 0.05 Debye/nm^2. On the contrary, through piling up B and C atoms together and placing N atoms on the top of hexagonal centers of graphene, the AB_N stacking geometry induces effective electron accumulation and depletion in h-BN layer and graphene, respectively, to generate a larger downward interlayer electric polarization of -0.2 Debye/nm^2 (as shown in Fig. S3d). Indeed, such non-negligible stacking-symmetry induced 2D ferroelectricity plays a key role to control the lateral alignment during growing few-layer h-BN sheets.

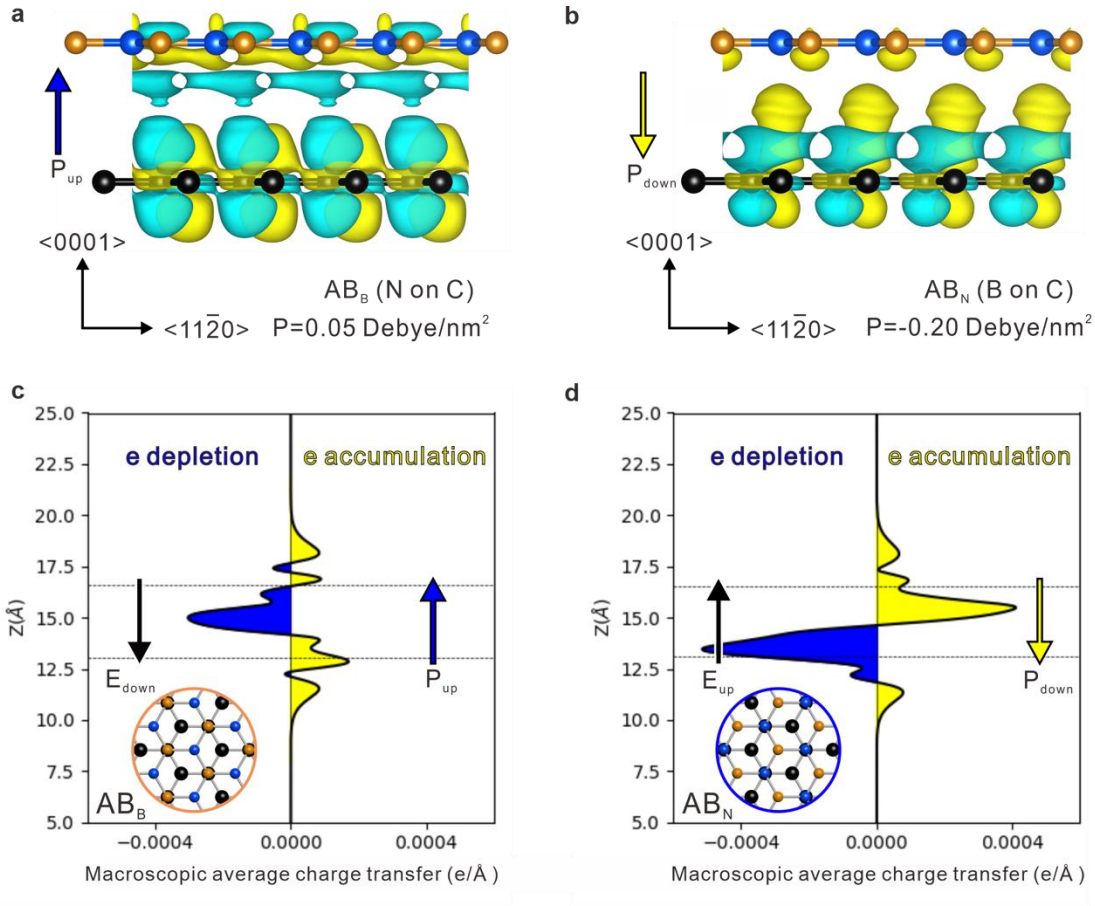

Figure S3 | Charge density analysis in different stacking configurations of h-BN/graphene. Interlayer differential charge density of h-BN on graphene in a. AB_B and b. AB_N stacking configurations. Electron depletion and accumulation is represented by cyan and yellow iso-surfaces with a value of 3.5 x 10^{-5} e/bohr^3, respectively. N, B, and C atoms are represented by orange, blue, and black spheres, respectively. The corresponding direction of interlayer polarization can be determined from the line profile along out-of-plane (z) direction in c. AB_B and d. AB_N, respectively. The integrated electron depletion and accumulation along the z direction of a large unit cell with a 30 Å c-axis including a 26 Å vacuum space are depicted in blue and yellow areas, respectively. The position of an individual layer is indicated by horizontal dotted line for reference.

S1.4. Raman spectroscopy of epitaxial h-BN

Raman spectra in multilayer graphene/SiC (black line) show characteristic graphene G band at 1590 cm^{-1} and 2D band in 2735 cm^{-1}, and the other peaks at 1400 cm^{-1}, 1516 cm^{-1} and 1707 cm^{-1} results from SiC substrate (Fig. S4a). Though there does not exist graphene D band in pure graphene substrate, during the h-BN growth process, graphene substrate was bombarded directly by nitrogen plasma, thus generating D band in h-BN/graphene sample. Therefore, the characteristic E_{2g} in-plane phonon vibration mode in few layers h-BN (red line) located at about 1371 cm^{-1}, but the Raman measurement actives not only phonon vibration mode in h-BN, but also graphene and SiC substrate, thus the broadband signal at 1371 cm^{-1} is an integration of h-BN E_{2g} and graphene D band. Nevertheless, the asymmetry of broadband signal is still able to be separated into h-BN E_{2g} located at 1371 cm^{-1} and graphene D band located at 1348 cm^{-1} (Fig. S4b). Note we transfer h-BN/graphene and h-BN onto SiO_2 substrate. Raman measurement in pure h-BN sample transfer on SiO_2 shows h-BN E_{2g} at 1363 cm^{-1} without graphene G or 2D band. Please refer to section **S4. Additional data**.

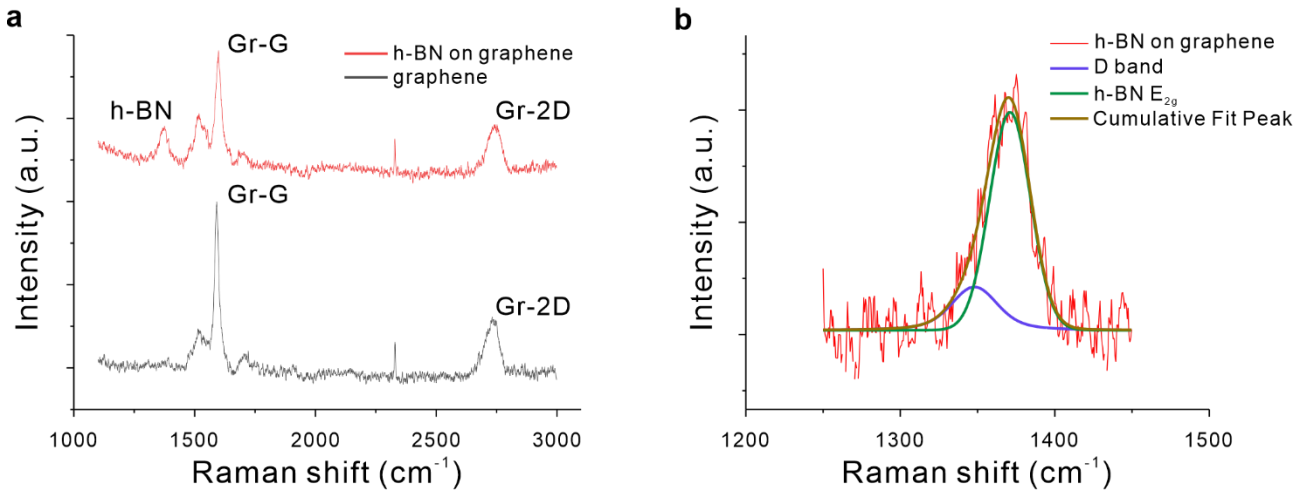

Figure S4 | Raman spectra of epitaxial h-BN. a, Raman spectra of h-BN/graphene (red) and multilayer graphene (black). **b**, Raman spectroscopy of characteristic h-BN E_{2g} in-plane phonon vibration mode integrated with graphene D band.

S2. ARPES characterization and first-principles band-structure calculations of the epitaxial growth of multilayer h-BN on graphene

S2.1. Comparison to monolayer, bilayer, and trilayer h-BN

In the main text, we briefly discussed the layer-dependent of electronic structure for h-BN/graphene. To achieve a detailed understanding of the layer-resolved band structures of h-BN on graphene, we measured ARPES spectra of h-BN/graphene along a high-symmetry path (M-Γ-K-M) of the Brillouin zone (BZ) with thickness ranging from mono- to tri-layer h-BN, as shown in Fig. S6 a1-c1. The 2nd derivatives of corresponding ARPES spectra were also performed, as shown in Fig. S6 a2-c2, for the enhancement of band dispersions which helps identifying the π bands with small splitting in multilayer h-BN. Since the intensity of photoelectron depends on the incident photon energy, beam polarizations, the penetration depth, etc., photoelectrons escaped from graphene will be attenuated by the surface coverage of h-BN layers, and become weaker as increasing the thickness of h-BN.

The intensity of ARPES spectra is governed by the product of a matrix element squared and a spectral function. The matrix-element term $M_{f,i}^{k}$ is defined by $\langle \Psi_f(\vec{k}_f)|H_{int}|\Psi_i(\vec{k}_i)\rangle$, in which $\Psi_f(\vec{k}_f)$, $\Psi_i(\vec{k}_i)$ are wave functions of the final and initial states, respectively[2]. In graphene-related systems, especially for bi- and tri-layer, the strength of photoemission intensities for π bands acts as an oscillating behavior with varied incident photon energies, which can attribute to the interference of photoelectron amplitudes emitted from individual layer[3,4]. The matrix element effect of π bands on bi- and tri-layer h-BN for different incident photon energies has been found in our layer-controllable h-BN sample (Fig. S7). The unchanged band dispersion on bi- ((Fig. S7a and S7c) and tri-layer h-BN (Fig. S7b and Fig.d) for varying incident photon energies suggests a 2D behavior of measured band structure. Moreover, the photoemission intensity of an individual splitting π band for bi- and tri-layer h-BN could be enhanced by different incident photon energies. That allows us to extract the band dispersion properly and to compare with the calculated band structure.

The epitaxial growth h-BN on graphene substrate samples in our systems involves van der Waals stacking. While the band gap cannot be determined properly through photoemission experiment and there are various reported band gap values, it is possible that the interlayer interactions between h-BN and graphene exist and trigger possible charge transfer behavior in our h-BN/graphene samples. In presented work, the valence band maximum (VBM) of π band in monolayer h-BN located at the K is

approximately 2.9 eV below the Fermi level, which differs from the reported values of monolayer h-BN prepared on various structures[5-7]. The difference between our work and previous reports could be attributed to the interlayer orbital hybridization between h-BN and various substrates, which could affect the size of band gap and doping situation.

S2.2. The effects of stacking configurations on multilayer h-BN

The band structures of few layer h-BN have been widely studied. It has been recognized that the degeneracy and dispersion of top-valence and bottom-conduction bands near K are sensitive to the symmetry of various stacking configurations[8]. Here, we report the band structures of AB and AA' stacking of free-standing bi-layer h-BN in both DFT and GW levels. Based on symmetry considerations, the band-crossing features of bands near the Fermi level at K point of AA' stacking (Fig. S5a) have been removed according to the geometrical symmetry breaking in AB stacking (Fig. S5b). Meanwhile, the location of valence band maximum (VBM) is slightly displaced from the high-symmetry K point while transferring from AB stacking into AA' stacking geometry. Moreover, the DFT-calculated indirect band gap value of 4.53 eV (4.59 eV) along the K-M path has been significantly corrected by GW-calculated one of 7.05 eV (7.06 eV) along the K-Γ path in AA' (AB) stacking, as indicated by dashed and solid arrows in Fig. S5.

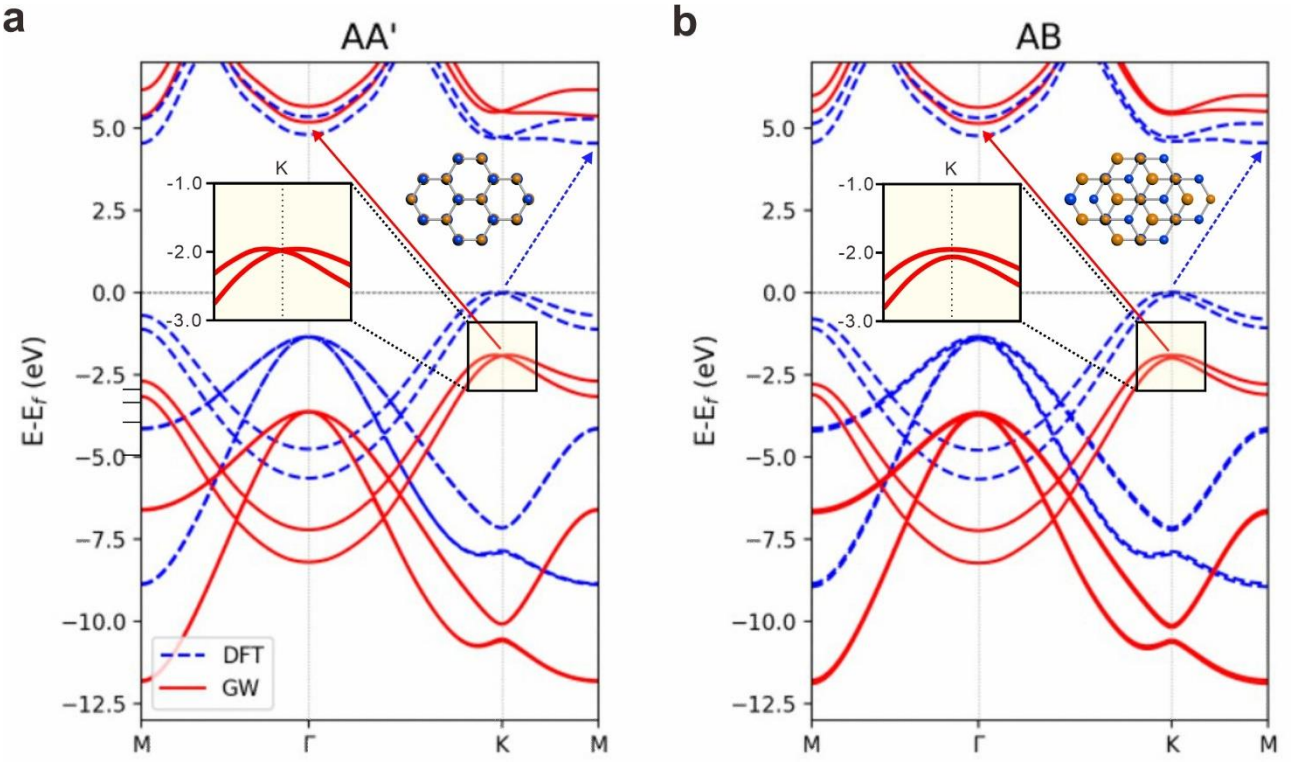

Figure S5 | Electronic band structures of AB and AA' stacking bilayer h-BN. DFT and GW calculated band structures of **a**, AA' and **b**, AB stacking configurations are denoted as blue dashed and red solid curves, respectively. Inset in a and b indicate the cross and split feature of AA' and AB stacking h-BN at K point. The indirect band gaps are indicated by corresponding colored arrows. The eigenvalues are all aligned with the Fermi level (dotted line) of DFT calculations. The models of different stacking sequences including B (orange spheres) and N (blue spheres) atoms in the bottom (larger spheres) and top (smaller spheres) layers are displayed in the insets.

S2.3. The influence of interlayer hybridization on h-BN/graphene heterostructures

In order to unveil the substrate effects and possible interlayer orbital hybridizations, a comprehensively study including experimental ARPES spectra and theoretical (in both DFT and GW approximation) band structures of multilayer h-BN with and without graphene substrate was demonstrated (Fig. S6). Qualitatively speaking, GW calculated band structures of free-standing systems (Fig. S6 a3-c3) agree fairly well with the original and 2nd derivatives of ARPES spectra (Fig. S6 a1-c1 and a2-c2). Nevertheless, our GW calculations including graphene substrate present significant modifications of band gap values (as listed in Table S.I) and more accurate band

dispersions while comparing with ARPES spectra of multilayer h-BN on graphene. On the other hand, the maintenance of the unique feature, Dirac cone, of graphene implies the interlayer coupling by means of vdW interactions may not be severe. However, a considerable interlayer orbital hybridizations among the π bands of graphene and h-BN layers has been recognized in the orbital projected band structures in GW level (Fig. S6 a4-c4). This unique interlayer hybridization in 2D heterostructures fosters the formation of moderate intrinsic interlayer charge transfer as discussed in section S1.3.

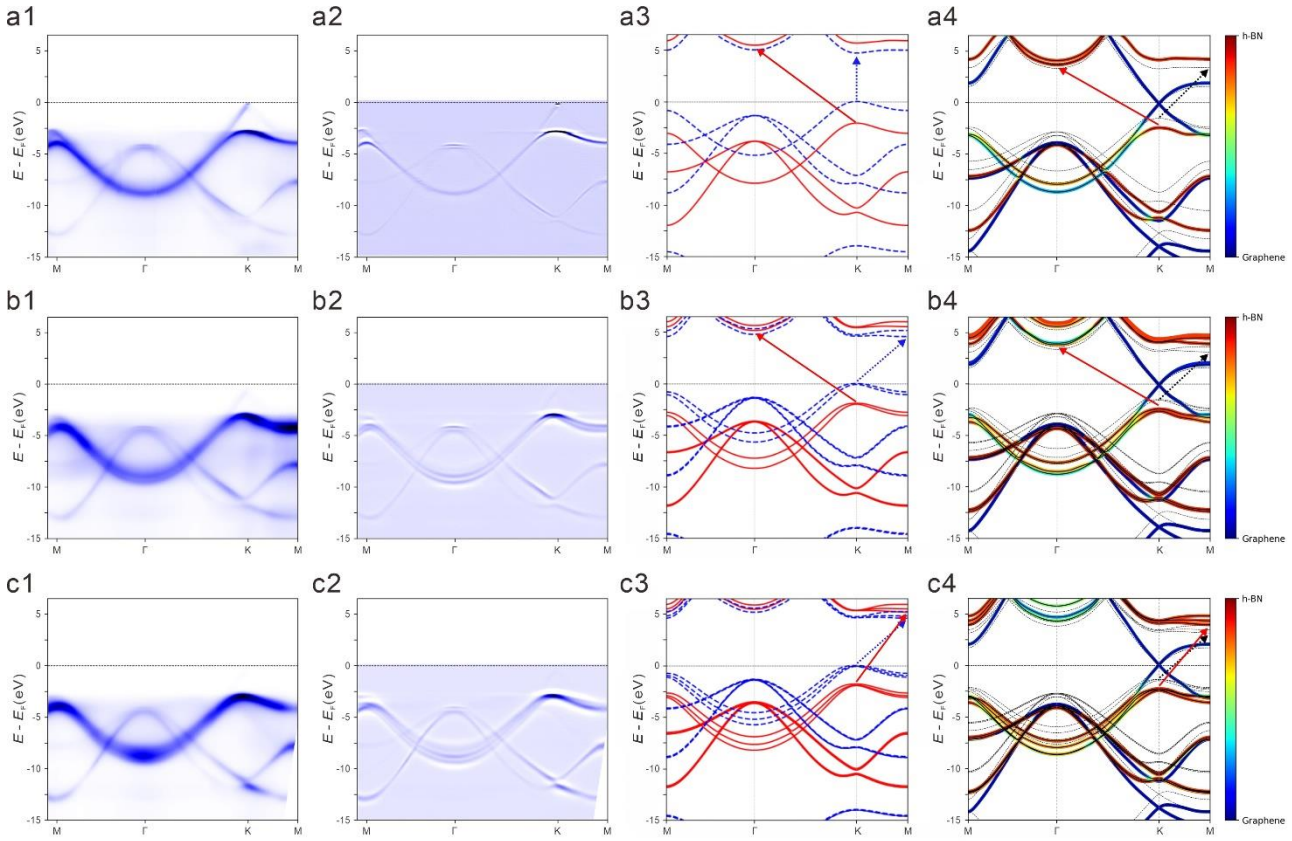

Figure S6 | Electronic band structures of h-BN and h-BN/graphene. a1-c1, ARPES spectra of mono-, bi- and tri-layer h-BN/graphene. **a2-c2**, The corresponding 2nd derivatives of ARPES data in **a1-c1**. **a3-c3**, Electronic band structures of free-standing mono-, bi-, and tri-layer h-BN in DFT (blue dashed curves) and GW (red solid curves) level calculations. **a4-c4**, Orbital projected GW band structures for h-BN (red) and graphene (blue) lateral heterostructures. All band energies are aligned with the Fermi level depicted as a horizontal black dashed line.

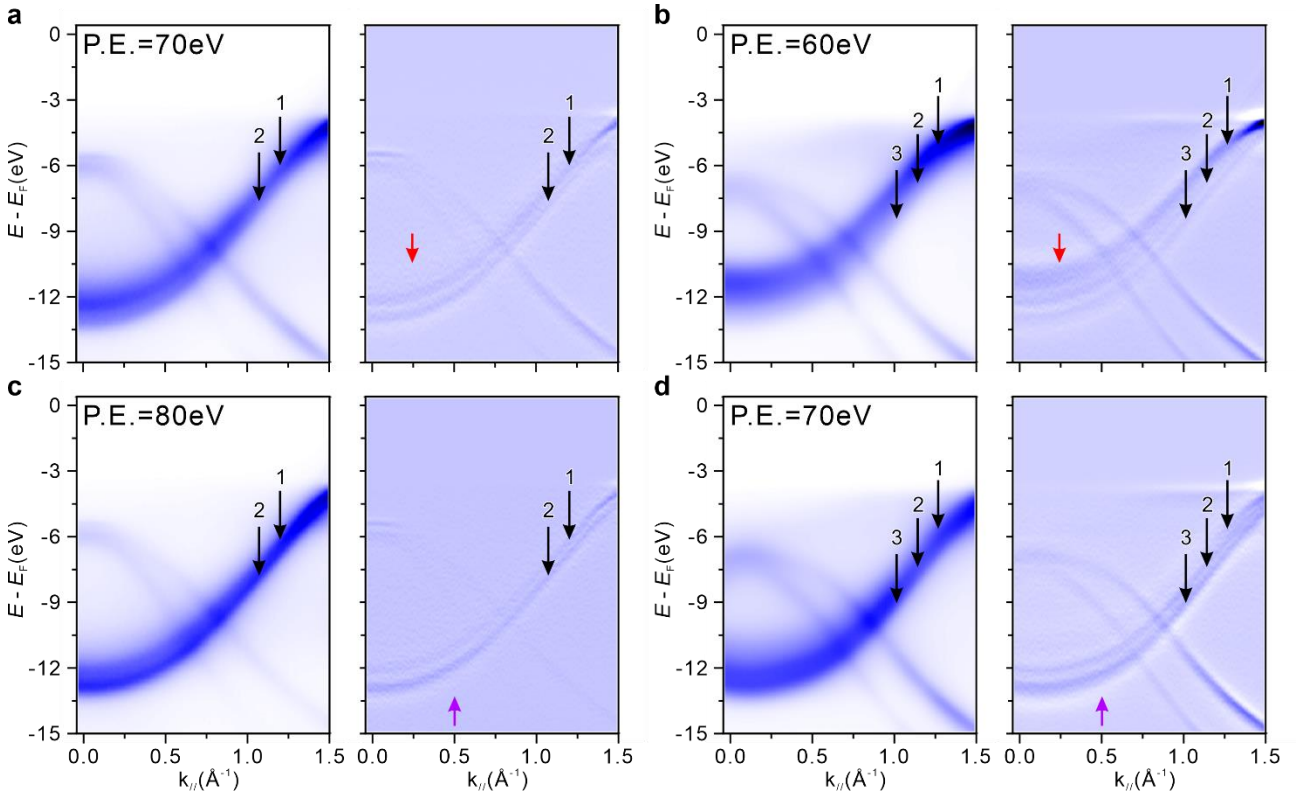

Figure S7 | Photon energy dependent ARPES spectra of bilayer and trilayer h-BN. a and **c**, bilayer h-BN ARPES spectra in Γ-K direction measured with 70eV and 80eV incident beam. **b** and **d,** trilayer h-BN ARPES spectra in Γ-K direction measured with 60eV and 70eV incident photon energies. Red and purple arrows indicate the higher photoemission intensity π band signals.

Table S. I Calculated band gap values with corresponding direct/indirect characters of multilayer h-BN with and without graphene substrate. Both DFT and GW calculated data are listed for comparison.

Mono-layer h-BN	With graphene substrate		Free standing	
	Gap (eV)		Gap (eV)	
DFT	4.81	Direct (K → K)	4.69	Direct (K → K)
GW	6.12	Indirect (K → Γ)	7.36	Indirect (K → Γ)
Bi-layer h-BN	With graphene substrate		Free standing	
	Gap (eV)		Gap (eV)	
DFT	4.61	Indirect (K → M)	4.55	Direct (K → K)
GW	6.26	Indirect (K → Γ)	7.05	Indirect (K → Γ)
Tri-layer h-BN	With graphene substrate		Free standing	
	Gap (eV)		Gap (eV)	
DFT	4.49	Indirect (K → M)	4.49	Indirect (K → M)
GW	6.37	Indirect (K → M)	6.88	Indirect (K → M)

S3. Electric field at step edges.

In our experiment, there is an intrinsic polarization field induced by well-aligned h-BN/graphene Moiré bands which has been investigated and measured by Zhiren Zheng *et al.*[9]. We take their experimental value, 0.05 μC/cm^2, into a corona discharge model to estimate the electric field at step-edge. The model is derived from classical electrodynamic[10]. Assume two conductive planes intersect with an angle β, charge will redistribute therefore causing a non-homogeneous electric field at the corner. The general solution of potential will be:

$$\Phi(r,\varphi) = V + ar^{\left(\frac{\varphi}{\beta}\right)} sin\frac{\pi\varphi}{\beta}$$

The electric field (E-field) is negative gradient of potential, $-\bar{\nabla}\Phi(r,\varphi)$, so there will be two orthogonal E-field:

$$\boldsymbol{E_r}(r,\varphi) = -\frac{\pi a}{\beta} r^{\left(\frac{\varphi}{\beta}\right)-1} sin\frac{\pi\varphi}{\beta}$$

$$\boldsymbol{E_\varphi}(r,\varphi) = -\frac{\pi a}{\beta} r^{\left(\frac{\varphi}{\beta}\right)-1} cos\frac{\pi\varphi}{\beta}$$

If β = π, two planes become one plane, $\boldsymbol{E_r}(r,\varphi)$ become constant a and independent of r, which correspond to the boundary condition, E-field at flat region. So constant a is -0.05 μ. The strongest or weakest E-field will be occurred at $\varphi = \frac{\beta}{2}$ when r is small, and the vdW spacing is approximately 0.33 nm, take $\varphi = \frac{\beta}{2}$ and $r = 0.33$ nm into $\boldsymbol{E_r}(r,\varphi)$, we can get the relation between E-field and bending angle at the corner (Fig. S8). The E-field value 1.0E-10 C/m^2 at bending angle $\frac{7}{6}\pi$ we take is obtained from TEM image (Fig. 3a).

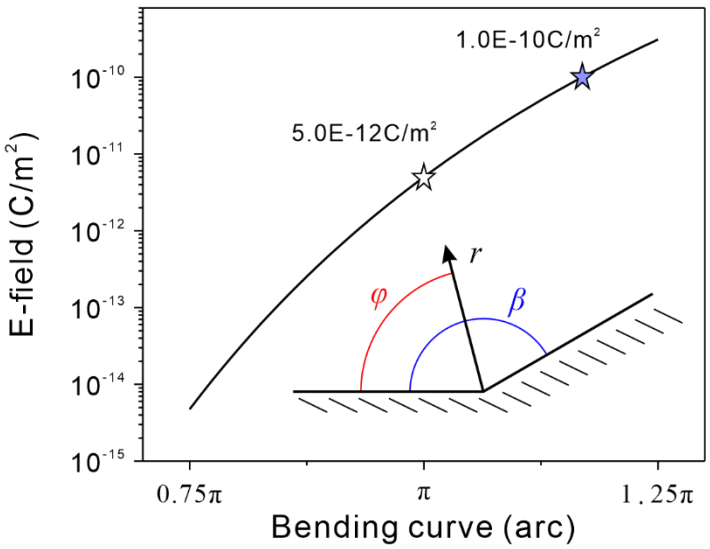

Figure S8 | Corona discharge effect. Corona discharge effect induced by two charged planes with an angle β. The electric field at $\varphi = \frac{\beta}{2}$ and $r = 0.33$ nm will be increase or decrease with a power law when β is bigger or small than π. White star is the electric field of infinite plane ($\beta = \pi$); blue star is the electric field at the joint of waning slope side and steep slope side.

S4. Additional Data – MBE-grown h-BN transferred on the SiO_x substrate

Because of the nature of van der Waals epitaxial growth in this study, we can transfer epitaxially grown h-BN/graphene onto a SiO_2 substrate by using the dry transfer technique. h-BN/graphene and h-BN were transferred onto a 300-nm SiO_2/Si substrate (Fig. S8a and S8b). A 3×8 mm h-BN epitaxially grown on graphene samples provides an opportunity to transfer large-scale h-BN onto the target substrate. We use polycaprolactone (PCL) to stick and transfer h-BN using the micromechanical exfoliation method. However, it is difficult to control the layer number of exfoliated h-BN/graphene. The coverage of h-BN on graphene is crucial in separating pristine h-BN from graphene. h-BN/graphene transferred onto SiO_2 was prepared from a 0.9-monolayer coverage h-BN on a graphene sample (Fig. S8a) and pristine h-BN transferred onto SiO_2 was prepared from a 3.3-monolayer coverage h-BN on a graphene sample (Fig. S8b). The Raman signal of pristine h-BN shows no graphene G and 2D band, exhibiting only a symmetrical Gaussian shape signal, indicating the appearance of only a single phonon vibration mode (red dots in Fig. S8c).

To investigate the topography of transferred h-BN/graphene, we conducted AFM experiments and found that the surface morphology was that of a compressed version of h-BN/graphene/SiC. The saw-toothed topography became flattened but retained a step-edge characteristic (Fig. S9a). The height (Fig. S9b) and adhesion channel (Fig. S9c) in the AFM results reveal a moiré lattice with a 14 nm period (Fig. S9d), suggesting there was no twisting between h-BN and graphene during the transfer process. This result supports the idea that we can transfer our epitaxially grown h-BN/graphene to other substrates by PA-MBE and offers an opportunity to create electronic devices by photolithography.

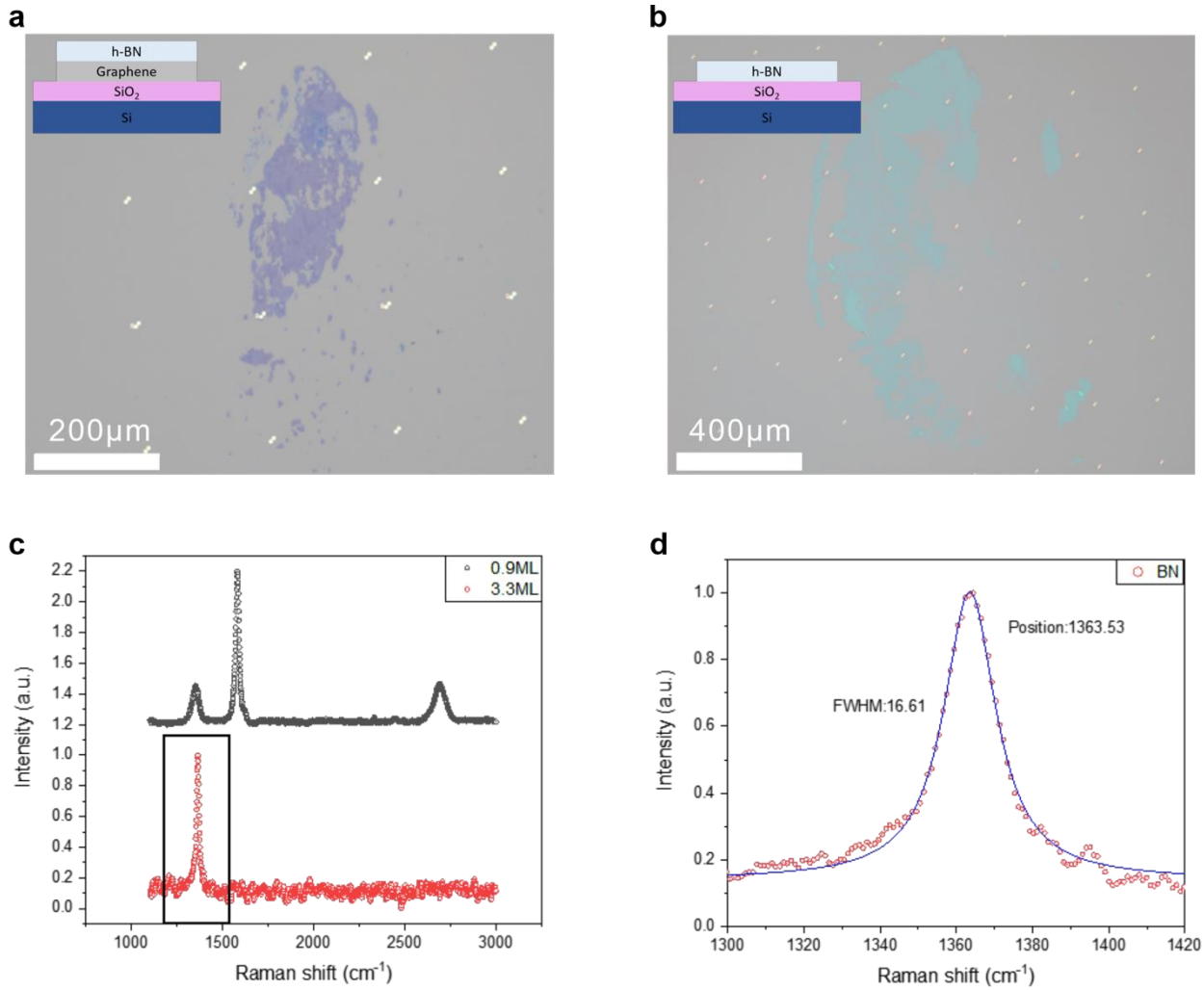

Figure S8 | Transferred h-BN and h-BN/graphene on the SiO_2 substrate. a, Optical image of h-BN/graphene on SiO_2 (transferred from 0.9-layer h-BN). **b**, Optical image of h-BN on SiO_2 (transferred from 3.3-layer h-BN). **c**, Raman spectra of h-BN/graphene (black line, measured from **a**) and h-BN (red line, measured from **b**). **d**, Characteristic h-BN E_{2g} in-plane Raman signal.

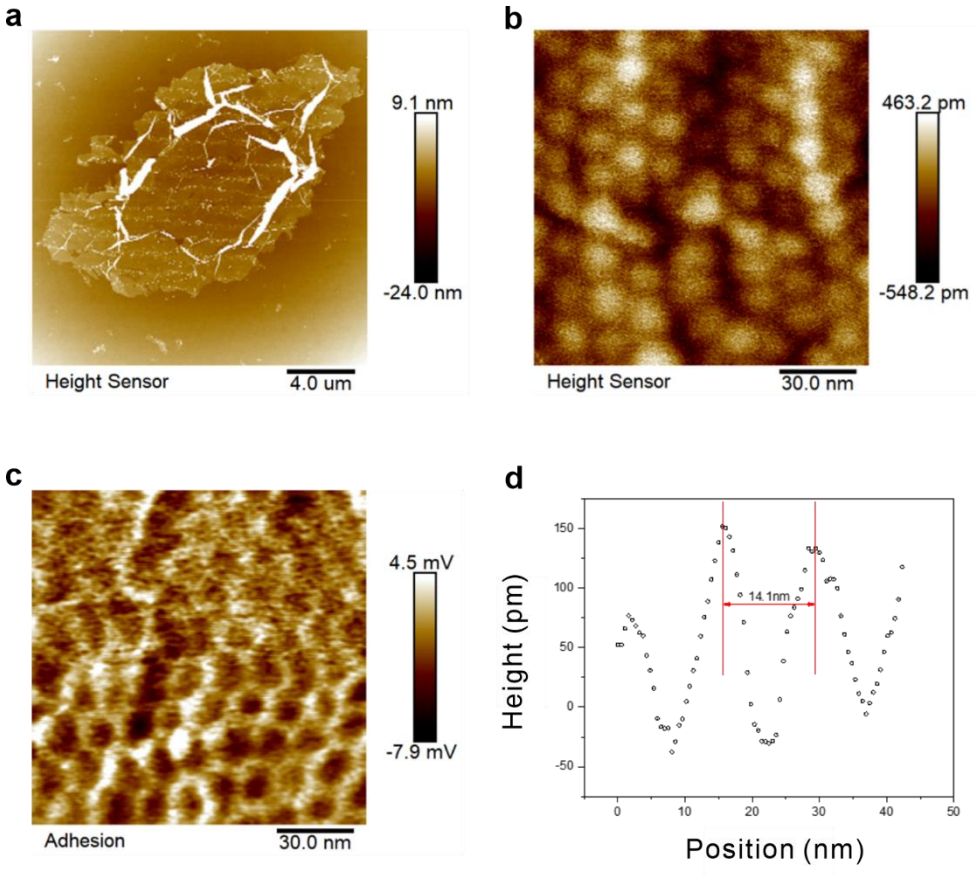

Figure S9 | Topographic images of h-BN/graphene transferred onto the SiO_2 substrate. a, Transferred h-BN/graphene fragment on SiO_2. **b**, Height and **c**, adhesion channel of h-BN/graphene on SiO_2. **d**, Line profile of transferred h-BN/graphene. The same 14-nm period moiré lattice is compared to the cAFM and PFM results in Figs. S2**d** and S2**e**.

Reference

1. Emtsev, K.V., et al., Towards wafer-size graphene layers by atmospheric pressure graphitization of silicon carbide. *Nat. Mater*. **8** 203-207 (2009)
2. Andrea D., Probing the Electronic Structure of Complex Systems by ARPES. *Phys. Scr.* **T61** 61-74 (2004)
3. Eric L. Shirley, L. J. Terminello, A. Santoni, and F. J. Himpsel. Brillouin-zone-selection effects in graphite photoelectron angular distributions. *Phys. Rev. B* **51**, 13614 (1995)
4. Ozaki, T., Variationally optimized atomic orbitals for large-scale electronic structures. *Phys. Rev. B* **67** 155108 (2003)
5. M. Petrović, Sequential lithium deposition on hexagonal boron nitride monolayer on Ir(111): Identifying intercalation and adsorption, *Surf. Sci.* **706** 121786 (2021)
6. A. Nagashima, N. Tejima, Y. Gamou, T. Kawai, and C. Oshima, Electronic states of monolayer hexagonal boron ni tride formed on the metal surfaces, *Surf. Sci.* **357**, 307 (1996).
7. D. Usachov et al., Quasifreestanding single-layer hexagonal boron nitride as a substrate for graphene synthesis. *Phys. Rev. B* **51**, 13614 (2010)
8. K. A. Mengle and E. Kioupakis, Impact of the stacking sequence on the bandgap and luminescence properties of bulk, bilayer, and monolayer hexagonal boron nitride, *APL Materials* **7**, 021106 (2019)
9. Zheng, Z., et al., Unconventional ferroelectricity in moire heterostructures. *Nature* **588**, 71-76 (2000)
10. Jackson, John David, 1925-2016. Classical electrodynamics. *New York :Wiley* (1999)